PHYSICAL SCIENCES

Necklace-structured high-harmonic generation for low-divergence, soft x-ray harmonic combs with tunable line spacing

Laura Rego[1]†, Nathan J. Brooks[2]†, Quynh L. D. Nguyen[2]*‡, Julio San Román[1], Iona Binnie[2], Luis Plaja[1], Henry C. Kapteyn[2], Margaret M. Murnane[2], Carlos Hernández-García[1]

The extreme nonlinear optical process of high-harmonic generation (HHG) makes it possible to map the properties of a laser beam onto a radiating electron wave function and, in turn, onto the emitted x-ray light. Bright HHG beams typically emerge from a longitudinal phased distribution of atomic-scale quantum antennae. Here, we form a transverse necklace-shaped phased array of linearly polarized HHG emitters, where orbital angular momentum conservation allows us to tune the line spacing and divergence properties of extreme ultraviolet and soft x-ray high-harmonic combs. The on-axis HHG emission has extremely low divergence, well below that obtained when using Gaussian driving beams, which further decreases with harmonic order. This work provides a new degree of freedom for the design of harmonic combs—particularly in the soft x-ray regime, where very limited options are available. Such harmonic beams can enable more sensitive probes of the fastest correlated charge and spin dynamics in molecules, nanoparticles, and materials.

INTRODUCTION

A new generation of coherent x-ray sources is opening up an advanced understanding of the fastest coupled charge, spin and phonon interactions, and transport in materials (1–5). X-ray sources such as free electron lasers (6, 7) and high-harmonic generation (HHG) (8–14) can produce coherent light from the extreme ultraviolet (EUV) to the soft x-ray (SXR) region. Moreover, in the case of HHG sources, they are perfectly synchronized to the driving laser, to subfemtosecond precision, and present high temporal coherence. In HHG, an atom undergoes strong field ionization in an intense femtosecond laser field. The liberated electron is then accelerated in the laser field before recombining with the parent ion, which results in the emission of higher-order harmonics. In the microscopic quantum picture, the driving laser creates a nanoscale dipole antenna in each atom, which radiates high harmonics of the fundamental laser field. This short wavelength radiation can be manipulated at the single atom level or at the macroscopic phase-matching level by structuring the intensity, frequency content, polarization, and orbital angular momentum (OAM) of the driving laser field (15–21).

Currently, control of the frequency content of the HHG light source—a key property for many advanced applications—is gained by changing the wavelength of the driving laser or by using frequency-selective optics or monochromators. By tuning the driving laser wavelength from the mid- and near-infrared (IR) to the ultraviolet, the HHG spectrum can be tuned from a bright coherent super-continuum to a set of narrow band (22, 23). Bright high-order harmonics extending into the keV region, well beyond the water window, can be obtained by using mid-IR driving fields (22, 24–30). Narrow spectral peaks into the SXR region can be achieved by

driving harmonics with UV lasers, although the low ponderomotive energy ($\sim\lambda^2$) necessitates the use of extremely high laser intensities (23). The manipulation of the frequency and the divergence of these HHG beams are still challenging and demand very efficient monochromators and good focusing optics in the EUV and SXR regions. An appealing alternative is to instead imprint the desired properties directly onto the HHG light, by tailoring the driving laser and taking advantage of selection rules. Recent works have demonstrated the relevance of nonperturbative dynamics underlying HHG in rephasing the wavefront to achieve good divergence profiles (31, 32), which can lead to focusing of harmonic beams without additional optics. However, it is still not possible to achieve general/full control over the frequency content and divergence properties of HHG radiation to tailor the HHG illumination for applications.

The emerging field of ultrafast structured light is providing exciting techniques for enhancing laser-matter interactions for applications (33). In particular, exploitation of the OAM is opening up unexpected avenues for controlling the properties of high-harmonic fields as they are being generated. OAM manifests itself as a variation of the beam's spatial phase along its transverse profile, and it is characterized by its topological charge, ℓ, or number of 2π phase twists along the azimuthal coordinate (34, 35). Since the first experiments in 2012 (36), OAM-driven HHG has proven to be a powerful tool for shaping the spatial properties of higher-order harmonics—including the topological charge, intensity distribution (37–42), and polarization properties (20, 43). OAM can also be used to control the temporal shape of HHG—through the generation of helical attosecond pulses (37, 39) or high harmonics with an OAM that increases during the pulse, which is a unique capability of HHG light (21). Although the ability to control the temporal shape implies an ability to also control the spectral shape, to date, OAM has not been yet exploited to tailor the spectral content in HHG.

In this work, we are able to control the spectral and divergence properties of HHG by driving it with optimally phased necklace laser beams—a class of ring-shaped beams with azimuthally modulated amplitude and phase, resulting from the interference of

multiple OAM modes. Our theoretical and experimental results show that by driving HHG with these structured beams, we generate a transverse phased array of HHG sources that emit a bright and adjustable harmonic comb along the optical axis. OAM selection rules and transverse phase-matching conditions allow us to tune the spectral spacing of these harmonics. Notably, the on-axis HHG emission has extremely low divergence, which is not only lower than that obtained with standard Gaussian beams, but the scaling behavior with the harmonic order is also reversed––such that higher-order harmonics exhibit progressively lower divergences (see Fig. 1). Our simulations demonstrate that these properties extend into the water window SXR regime, when driven by mid-IR necklace beams. This work provides a new degree of freedom for the design of harmonic combs—particularly in the SXR regime, where very limited options are available.

RESULTS

Modifying the high-harmonic line spacing through necklace-driven HHG

Necklace beams can be generated and maintained through self-focusing in nonlinear media (44, 45) or by creating them using either spatial light modulators (46) or specially tailored diffractive optical elements (47, 48). Here, we form necklace beams with a distinctive phase structure by spatiotemporally overlapping two femtosecond laser pulses with identical duration, wavelength, and polarization, but opposite and nondegenerate OAM ($\ell_1 = |\ell_1|$, $\ell_2 = -|\ell_2|$). The composite electric field exhibits a modulated intensity necklace structure, with evenly spaced lobes of similar amplitude arranged at a constant distance from the optical axis, and with a relative phase shift between neighboring lobes. Figure 1A shows the intensity-modulated phase profile at the focus resulting from the superposition of two vortex beams with $\ell_1 = 2$, $\ell_2 = -3$, as well as the far-field spatial intensity distribution of a given harmonic order (the 25th). Although the driving field contains a singularity and hence has zero intensity at all points along the optical axis, we observe numerically and experimentally that a subset of harmonic orders develops a bright on-axis maximum upon propagation. We further find that by using different combinations of OAM beams to synthesize the necklace driver, this subset can be varied, allowing us to tune the line spacing of the harmonic comb emitted on the optical axis without altering the driving laser wavelength.

This unexpected result can be understood by viewing the combined dual-vortex source as an EUV/SXR phased antenna array.
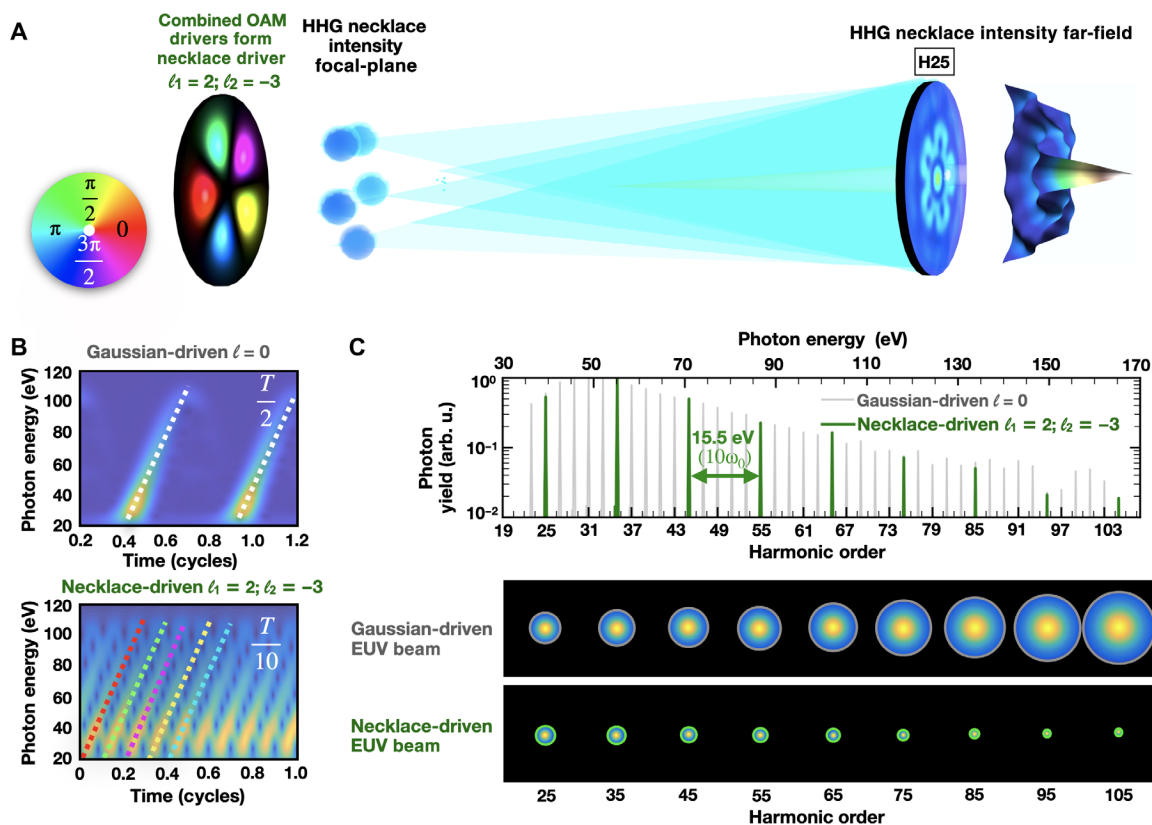

Fig. 1. Tunable, low-divergence high-harmonic combs via necklace-driven HHG. (**A**) Two linearly polarized vortex beams carrying OAM of $\ell_1 = 2$ and $\ell_2 = -3$ are overlapped to create a necklace-structured intensity and phase profile and focused into He/Ar gas to drive HHG. The intensity lobes at the necklace focal plane represent a phased array of EUV/SXR emitters, which interfere on-axis to form a comb of harmonics with a spacing dependent on the OAM of the driving fields. The harmonic intensity profile shows a strong emission on-axis (detailed in the figure for the 25th harmonic). (**B**) Time-frequency analysis of the simulated on-axis harmonic comb for Gaussian- and necklace-driven ($\ell_1 = 2$, $\ell_2 = -3$) HHG in He at 800 nm. The dashed color lines indicate the corresponding phase from (A) for each emission event. (**C**) HHG spectrum for the case of necklace- and Gaussian-driven HHG simulated in (B). The harmonic spacing, $\Delta\omega = 10\omega_0$ (15.5 eV), in the necklace-driven on-axis HHG spectrum is a result of OAM conservation and is tunable by varying the OAM content of the driving laser (top). The on-axis harmonics are emitted with a divergence, which is substantially reduced compared to that of Gaussian-driven HHG and decreases with increasing harmonic order (bottom).

The composition of OAM beams creates a necklace-structured electric field containing $N = |\ell_1| + |\ell_2|$ lobes equidistant from the optical axis/origin, where the relative phase offset of the fundamental field across the nth lobe is constant and equal to $(2\pi n |\ell_1|)/(|\ell_1| + |\ell_2|)$ (see the Supplementary Materials). Treating each lobe as a radiator of the qth-order harmonic, which is coherent with the driving laser, the total field at a point $\vec{r}_f$ away from the source plane is the sum of fields propagated from all the lobes in the necklace and can be approximated by

$$E_q(\vec{r}_f, t) \propto \sum_{n=0}^{N-1} e^{i\left(q\omega_0 t + q k_0 d_n + 2\pi n \frac{q|\ell_1|}{|\ell_1| + |\ell_2|} \right)} \quad (1)$$

The second phase term $q k_0 d_n$ describes the phase accumulated by the qth harmonic propagating a distance $d_n = |\vec{r}_f - \vec{r}_{0,n}|$ from the nth lobe to the observation point. Let us now consider the harmonic emission that is emitted on-axis. For all points lying along the optical axis, these $d_n = d$ are equal. Thus, the propagation amounts to a constant phase shift (independent of n), which we can omit without loss of generality. The final phase term can be simplified by reordering the terms in the summation, yielding (see the Supplementary Materials)

$$E_q(\vec{r}_{\text{on-axis}}, t) \propto e^{iq\omega_0 t} \sum_{n=0}^{N-1} e^{i2\pi n \frac{q}{\xi_1 + \xi_2}} \quad (2)$$

where we have introduced $\xi_1 = L_{\text{lcm}}/|\ell_1|$ and $\xi_2 = L_{\text{lcm}}/|\ell_2|$, with L_{lcm} being the least common multiple of $|\ell_1|$ and $|\ell_2|$. From the above equation, we can observe that, for harmonics where the quantity $q/(\xi_1 + \xi_2)$ is an integer, the emission from all lobes arrives in phase, resulting in a maximum on axis, while for all other harmonics the contributions sum to zero. In other words, for certain harmonic orders, the transverse phase matching of the harmonic emission at the different lobes results in a constructive interference in the far-field optical axis. Taking into account the additional constraint that q must be odd due to inversion symmetry results in an HHG comb with line spacing equal to

$$\Delta\omega = 2(\xi_1 + \xi_2)\omega_0 \quad (3)$$

The temporal counterpart of this modified line spacing manifests in the periodicity of harmonic emission recorded on the optical axis. In Fig. 1B, we perform a time-frequency analysis of the on-axis harmonic signal extracted from our simulation results in He at 800 nm (see theoretical methods below). We compare the harmonic emission driven by a standard Gaussian beam against that driven by a necklace beam with OAM content $\ell_1 = 2$, $\ell_2 = -3$. For the Gaussian driving beam, harmonics are emitted every half period of the driving field, showing a periodicity of $\Delta t = T_0/2$ (where $T_0 = 2\pi/\omega_0$ is the optical cycle associated to the central frequency of the driving field), which physically corresponds to the cadence of the ionization-rescattering mechanism leading to HHG. This structure corresponds to a harmonic frequency comb composed of odd harmonics, with spacing $\Delta\omega = 2\omega_0$ (see Fig. 1C). However, for the combined $\ell_1 = 2$, $\ell_2 = -3$ OAM driving field, harmonic events are observed on-axis 10 times—i.e., $2(\xi_1 + \xi_2)$—per period of the driving frequency, reflecting the coherent addition of the 5—$\xi_1 + \xi_2$—unique HHG emitters in the necklace. As a consequence, the on-axis harmonic emission shows a periodicity of $\Delta t = T_0/10$—$\Delta t = T_0/2(\xi_1 + \xi_2)$—corresponding to a harmonic frequency comb with the line spacing given by Eq. 3. We emphasize that this is accomplished

without altering the wavelength of the driving laser or the microscopic dynamics. The spectral changes arise purely as a result of the macroscopic arrangement of the phased emitters.

A deeper understanding of the modified harmonic comb spacing can be gained by invoking the selection rules resulting from OAM conservation. HHG driven by two spatiotemporally overlapped OAM pulses leads to the generation of a comb of harmonics with several, nontrivial, OAM contributions (40). In particular, neglecting the intrinsic or dipole phase contributions (40), the qth-order harmonic order has allowed OAM channels given by $\ell_q = n\ell_1 + (q - n)\ell_2$, where n is a positive integer representing the number of photons of the ℓ_1 driver. If we apply this conservation rule to our scheme where the two drivers have opposite, nondegenerate OAM, i.e., $\ell_1 = |\ell_1|$ and $\ell_2 = -|\ell_2|$, we can readily observe that high-order harmonics emitted on-axis, i.e., with $\ell_q = 0$, are generated if $n|\ell_1| = (q - n)|\ell_2|$. To extract the allowed harmonics that fulfill this condition, and thus the content of the harmonic comb emitted on-axis, we again denote L_{lcm} as the least common multiple of $|\ell_1|$ and $|\ell_2|$, which fulfills $\eta L_{\text{lcm}} = n|\ell_1| = (q - n)|\ell_2|$, with η being an integer. Retaining the definitions of ξ_1 and ξ_2, the harmonic orders emitted with $\ell_q = 0$ must fulfill $q = \eta(\xi_1 + \xi_2)$. Taking into account that q must be odd due to the inversion symmetry, η must be odd, and the high-order harmonics that are emitted on-axis are

$$\omega_q = (2m + 1)(\xi_1 + \xi_2)\omega_0 \quad (4)$$

where $m = 0, 1, 2\ldots$, again leading to the line spacing rule given by Eq. 3.

The line spacing $\Delta\omega$ is shown in Fig. 2A in terms of $|\ell_1|$ and $|\ell_2|$. We see that the appearance of on-axis harmonics with modified spectral spacing is a necessary consequence of a fundamental conservation law for OAM in HHG, as the OAM content of the driver determines which harmonic wavelengths have an allowed $\ell_q = 0$ channel. This interpretation naturally implies that the intensity ratio between the driving beams can be chosen to optimize the $\ell_q = 0$ (on-axis) contribution (see the Supplementary Materials). Note that those harmonics that are not emitted on-axis have nonzero OAM, and although they are present in the HHG beam, they present a singularity at the center.

To verify these predictions, we performed full quantum HHG simulations including propagation using the electromagnetic field propagator (49) (see Methods), a method that was used in several previous calculations of HHG involving OAM (20, 21, 37, 40, 43). In Fig. 2 (B and C), we present the on-axis HHG spectra driven in He with 800-nm and 2-μm wavelength driving fields, respectively, and for different drivers' OAM combinations: $\ell_1 = 1$, $\ell_2 = -2$ (blue); $\ell_1 = 2$, $\ell_2 = -3$ (green); $\ell_1 = 3$, $\ell_2 = -4$ (yellow); and $\ell_1 = 4$, $\ell_2 = -5$ (red). In Fig. 2B, we also show the spectra obtained with a standard Gaussian beam driver (gray). The simulation results show the versatility of this technique to modify the frequency content of the harmonic combs, whose line spacing can be properly varied through the choice of the drivers' OAM, from $2\omega_0$ to $18\omega_0$ for the cases presented in Fig. 2.

By using mid-IR drivers, this technique can be exploited to customize harmonic combs extending into the SXR—as depicted in Fig. 2C, where photon energies of up to 640 eV are reached using 2-μm wavelength. This is particularly promising in a regime where, driven by long-wavelength Gaussian beams, neighboring harmonic orders tend to merge into a near or true supercontinuum (22, 23),
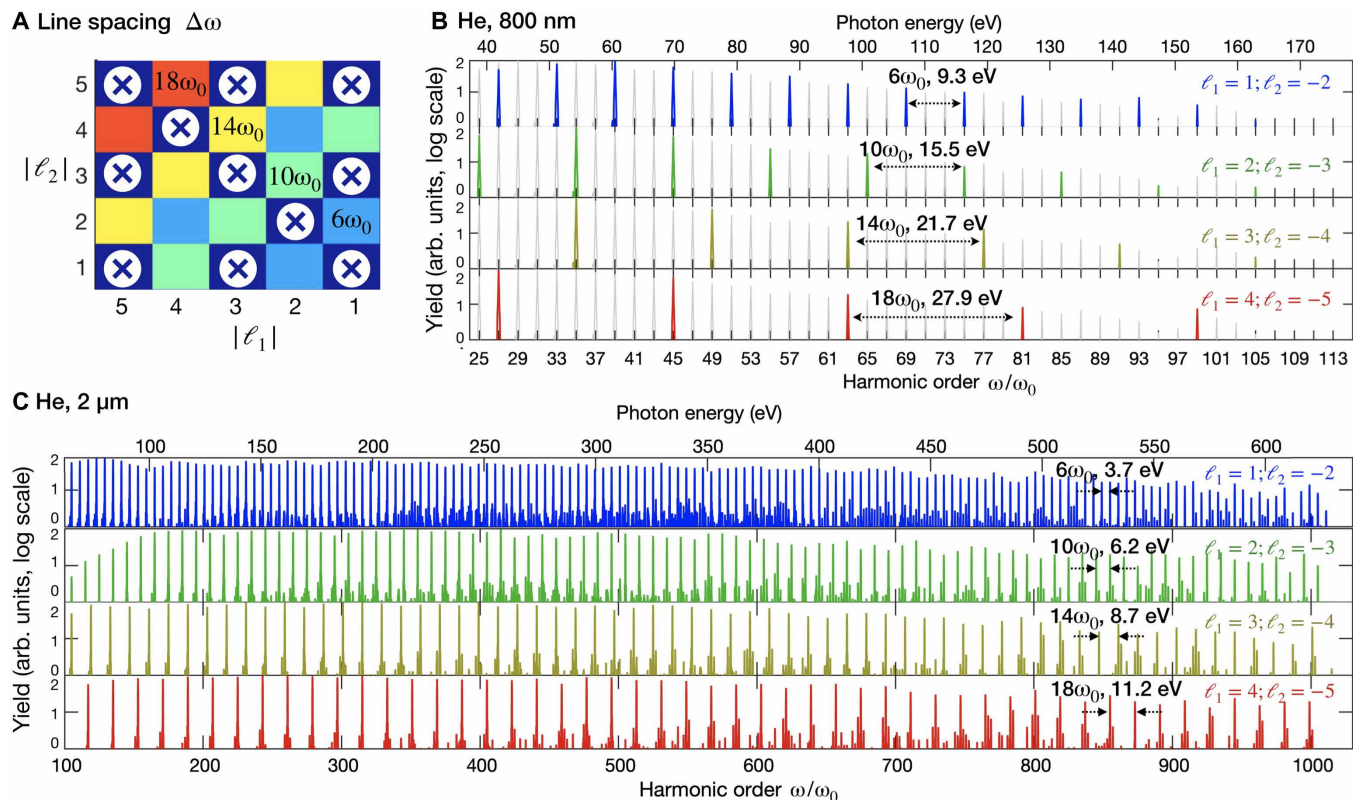
Fig. 2. Harmonic frequency combs with tunable line spacing controllable through the drivers' OAM content. (**A**) Representation of the line spacing allowed by the selection rules for different values of $|\ell_1|$ and $|\ell_2|$. The color scale represents the line spacing, being $6\omega_0$ (blue), $10\omega_0$ (green), $14\omega_0$ (yellow), and $18\omega_0$ (red). (**B** and **C**) Simulation results of the high-harmonic spectra obtained in He for (B) 800-nm and (C) 2-μm wavelength drivers, respectively, for the driver's OAM combinations: $\ell_1 = 1$, $\ell_2 = -2$ (blue); $\ell_1 = 2$, $\ell_2 = -3$ (green); $\ell_1 = 3$, $\ell_2 = -4$ (yellow); and $\ell_1 = 4$, $\ell_2 = -5$ (red). The line spacing corresponds to that predicted in (A). The driving beam waists of the different OAM modes are chosen to overlap at the radius ($30/\sqrt{2}$ μm) of maximum intensity (6.9×10^{14} W/cm² for 800 nm, and 5×10^{14} W/cm² for 2 μm) at the focal plane. The laser pulses are modeled with a trapezoidal envelope with 26.7 fs of constant amplitude.

necessitating the use of lossy dispersive optics for spectroscopic applications. In contrast, these simulation results demonstrate that, using necklace-driven HHG, the discrete and tunable peak structure can be preserved up to the SXR when driven by mid-IR wavelengths. Moreover, the mid-IR OAM-driven HHG necklace scheme can, in principle, be implemented in a waveguide, allowing for confined propagation that compensates for the low single-atom yield to achieve maximum flux. This capability opens previously unidentified avenues for element-specific spectroscopies and ultrafast spin dynamics of multilayer materials that consist of 3*d* transition metals. We note that the intensity ratio between the two driving pulses has been adjusted independently for each OAM combination to optimize the $\ell_q = 0$ contribution (see the Supplementary Materials). In addition, the driving beam waists of the different OAM modes are chosen so that their rings of maximum intensity overlap at $\rho_1 = 30/\sqrt{2} = 21.21$ μm at the focal plane (see Methods), corresponding to the ring of maximum intensity of a vortex beam with $\ell = 1$ with $w_0 = 30$ μm, used as a reference.

To experimentally confirm the predicted spectral properties of this unique EUV light source, we use a Mach-Zehnder interferometer to synthesize the necklace-structured driver from two OAM laser beams with identical wavelength $\lambda = 790$ nm and distinct topological charges of $\ell_1 = 1$, $\ell_2 = -2$ (see Methods). The component beams are overlapped in time and space and focused into an argon

gas jet to drive HHG. The spectrum and shape of the emitted harmonics are then analyzed via a 2D imaging spectrometer consisting of a toroidal mirror and flat grating. As the on-axis HHG beam component is predicted to develop through propagation away from the source, we place an EUV charge-coupled device (CCD) camera slightly behind the focal plane of the toroidal mirror. The measured spatiospectral images thus simultaneously record the harmonic photon energies and individual far-field spatial profiles.

The measured spatial intensity profile of each of the high-order harmonics presents a structure with a symmetry similar to that of the driving necklace beam, in agreement with the results from our theoretical simulations (see Fig. 3). In this OAM combination, the predicted line spacing of the on-axis harmonic comb is $\Delta\omega = 6\omega_0$ (9.5 eV), and the highest measurable harmonic orders allowed by the selection rule given by Eq. 2 are the 15th (23.5 eV) and 21st (33.0 eV) harmonics. This is supported by the intensity profiles shown in Fig. 3, where the central bright spot in the 15th and 21st harmonics indicates a strong on-axis ($\ell = 0$) component. In contrast, all other observed harmonic orders exhibit a central null, i.e., they only have nonzero OAM contributions that lead to off-axis emission profiles. To confirm that these features constitute the predicted harmonic combs with on-demand line spacing, we insert a small circular aperture into the HHG beam before the spectrometer. We observe that the harmonics with on-axis components are cleanly
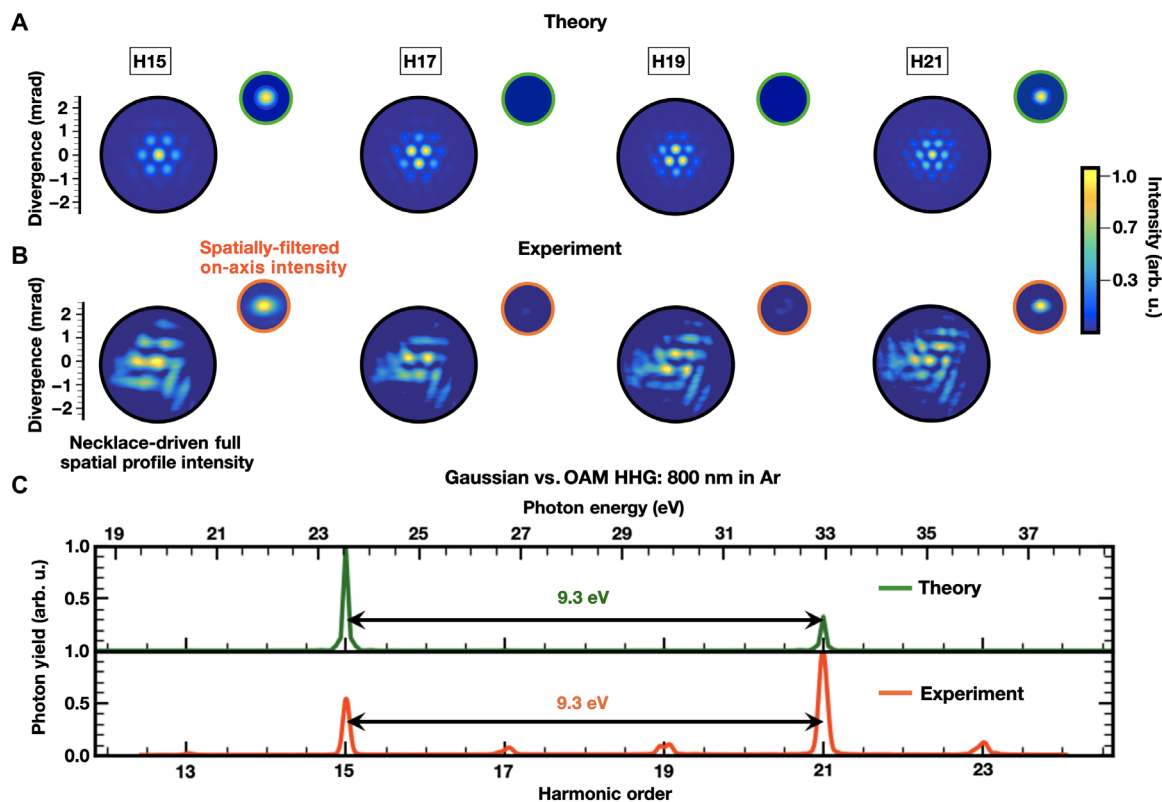
Fig. 3. Experimental and theoretical high-harmonic combs in Ar gas using a pair of 790-nm OAM driving lasers with opposite parity ($\ell_1 = 1$ and $\ell_2 = -2$). The intensity spatial structure for the 15th (H15) to 21st (H21) harmonics is shown for (**A**) theory and (**B**) experiment. On-axis emission is allowed for H15 and H21 as a result of OAM selection rules and transverse phase-matching conditions. Thus, the on-axis component is transmitted for H15 and H21, while H17 and H19 are blocked [insets in (A) and (B)]. (**C**) Simulated (top) and experimental (bottom) HHG spectra of necklace-driven on-axis emission. By measuring the spectrum along a line in the dispersion plane that intersects the optical axis for all orders, we find that the line spacing of the transmitted harmonics, $\Delta\omega = 6\omega_0$ (9.5 eV), is consistent with that predicted by OAM conservation laws. Small HHG signals experimentally observed at other harmonic orders are due to leak-through of the components carrying higher topological charges and could be further suppressed by using a smaller aperture. The difference in the ratio H15/H21 is due to slightly different cutoff energies between simulation and experiment.

transmitted through the aperture, while other harmonic orders are strongly suppressed. In the Supplementary Materials, experimental results for another phased-necklace driver ($\ell_1 = 2$, $\ell_2 = -3$) further support the predicted line spacing of the on-axis harmonic combs. We would like to point out that the suppression of the forbidden harmonics from our necklace driving beam is similar to what is usually obtained using bicircular driving beams (*18*, *50*, *51*), a very well established scheme that has been used for applications in spectroscopy.

Generation of low-divergence high-order harmonics via necklace-driven HHG

In addition to their spectral content, the divergence of the high-harmonic combs is also crucial for applications in x-ray spectroscopy and imaging. In our scheme, the on-axis harmonics with on-demand line spacing are generated with lower divergence, compared to that obtained from standard Gaussian driving laser beams. This is a consequence of the generation mechanism, in which the on-axis beam, not present in the source plane, arises from the constructive interference of multiple phased-shifted radiators arranged with circular symmetry about the optical axis. Figure 4A shows the simulation results of the spatial intensity profile (top) and OAM content (bottom) of the 27th harmonic generated in He at 800 nm for two

different OAM combinations: $\ell_1 = 1$, $\ell_2 = -2$ (left) and $\ell_1 = 4$, $\ell_2 = -5$ (right). It can be observed that most of the harmonic intensity is contained near the beam axis, corresponding to the $\ell_{27} = 0$ contribution. This is a result of the intensity ratio of the component OAM beams, which has been selected to optimize the channel for on-axis harmonic emission (see the Supplementary Materials), such that the surrounding OAM contributions are naturally suppressed (see OAM spectra in the bottom panels of Fig. 4A). This needle-like beam naturally separates from the driving laser, which has zero on-axis intensity, and can be easily isolated through a pinhole for direct use in an experiment.

To show the low divergence of the $\ell_q = 0$ harmonic beam, we present in Fig. 4B the divergence of the high-order harmonics driven by the opposite nondegenerate OAM combination (corresponding to those of Fig. 2B), compared to that of the harmonics driven by a Gaussian beam. We have chosen a beam waist of 30 μm for the Gaussian beam, as a reasonable comparison against the OAM combination scheme, where the necklace ring presents a radius of $30/\sqrt{2}$ μm. The insets show the divergence profile of two sample harmonics (27th and 45th) driven by different drivers' OAM combinations (the solid lines show the $\ell = 0$ contribution of each harmonic, whereas the dashed lines show the sum of all the OAM contributions) and by a Gaussian beam. Note that the intensity yield of the on-axis
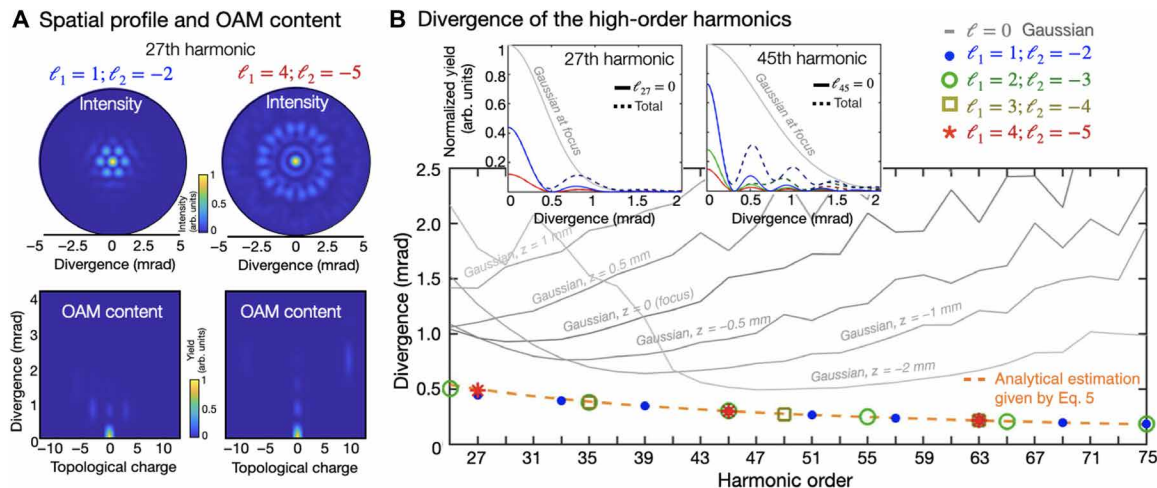
Fig. 4. Low divergence of the necklace-driven harmonic frequency combs. (**A**) Simulation results of the spatial intensity profile (top) and OAM content (bottom) of the 27th harmonic generated in He for $\ell_1 = 1$, $\ell_2 = -2$ (left) and $\ell_1 = 4$, $\ell_2 = -5$ (right) driving fields. The OAM spectra are obtained from the azimuthal Fourier transform at each divergence angle. (**B**) Simulation results of the full width at half maximum (FWHM) divergence of the high-order harmonics for different OAM driving combinations (color dots)—with the gas jet placed at the focus position—and for a Gaussian driving beam where the gas jet is placed at different positions relative to the focus: from 2 mm before the focus ($z = -2$ mm) to 1 mm after the focus ($z = 1$ mm). The orange dashed line indicates the estimation given by Eq. 5. The top insets show the divergence profile of two sample harmonics (27th and 45th) for different OAM driving combinations (showing the $\ell_q = 0$ contribution in solid and the total one in dashed line) and for a Gaussian beam where the gas jet is placed at the focus position. Simulation parameters correspond to those of Fig. 2B.

emission is comparable to the yield obtained with a Gaussian beam. The bottom panel shows the divergence calculated as the full width at half maximum for different drivers' OAM combinations (dots and dashed lines)—with the gas jet placed at the focus position—and for a Gaussian beam, with the gas jet placed at different positions relative to the focus (solid gray lines): before the focus ($z = -2$ mm, $z = -1$ mm, $z = -0.5$ mm), at the focus ($z = 0$ mm), and after the focus ($z = 0.5$ mm, $z = 1$ mm).

It is worth noticing that Gaussian-driven high-order harmonics, counterintuitively, exhibit a divergence that generally increases with the harmonic order (*31*, *32*). In such cases, the divergence of the central intensity peak of the qth harmonic scales as $\beta_q \sim \lambda_q/D_q$, where D_q is the size of the near-field target area in which the driving field is intense enough to generate that particular harmonic. The fact that D_q decreases with the harmonic order faster than λ_q results in an increasing divergence with the harmonic order, as can be observed in Fig. 4B. This behavior holds also when the gas jet is placed before the focus position ($z < 0$ mm), where lower divergences can be obtained due to the converging phase profile of the driving beam (*31*, *32*). Because of the use of an optimized phased-necklace driver, we are able to reverse this behavior. When considering the opposite nondegenerate OAM driving field, the divergence of the $\ell_q = 0$ intensity peak of the qth harmonic scales as

$$\Delta \beta_q^{\text{FWHM}} = 2.25 \frac{\lambda_0}{2\pi q R} \tag{5}$$

where R is the radius of the necklace driving structure (see the Supplementary Materials). The result is that higher-order harmonics can be generated with progressively lower divergence, as R is constant for all harmonic orders. Note also that this behavior does not depend on the choice of ℓ_1 and ℓ_2, but on the size of the resulting necklace structure, which, for the cases presented in Fig. 4B, presents the same size. As a consequence, similar driving schemes

without OAM, such as a Gaussian-necklace driver or a continuous-ring driver—which, to the best of our knowledge, have not been used before—would also result in on-axis high-order harmonics with progressively lower divergence. Note, however, that our phased-necklace driver is composed of a combination of Laguerre-Gaussian modes, whose propagation behavior is regular and which allow us to control the on-axis harmonic content as described in the previous section.

We experimentally validate the predicted divergence behavior of the HHG frequency combs for Ar at 790 nm in Fig. 5. Taking an angular integration centered about the optical axis for the necklace-driven HHG, and considering the imaging condition of the spectrometer, we measure the divergence of the on-axis, Bessel-like lobe. We then compare these divergence values to those obtained with an equivalent Gaussian driver. To make as direct a comparison as possible, we match the beam waist parameter (lens focal length), focal position, gas pressure, and peak intensity between the two cases, resulting in HHG spectra with similar spectral envelopes and cutoff photon energies.

From these spectra, we make several observations. First, it is clear that the central lobe of the necklace-driven harmonics with on-axis components has a notably lower divergence than that achievable with the equivalent Gaussian driver. Furthermore, we observe a clear decrease in the divergence of the 21st harmonic relative to the 15th harmonic, whereas the Gaussian harmonics, as expected, actually increase in divergence over the same energy range. Both the divergence values and trend quantitatively agree with our simulations, as well as the prediction given by Eq. 5. Last, we note that both our numerical and experimental results show that the on-axis harmonics are nearly equal in peak brightness to their Gaussian counterparts, indicating that the frequency selectivity and low divergence achieved in this scheme do not come at the cost of reduced flux at those frequencies. Note that the brightness of the on-axis harmonics can be controlled through the intensity ratio between the drivers (see the Supplementary Materials).
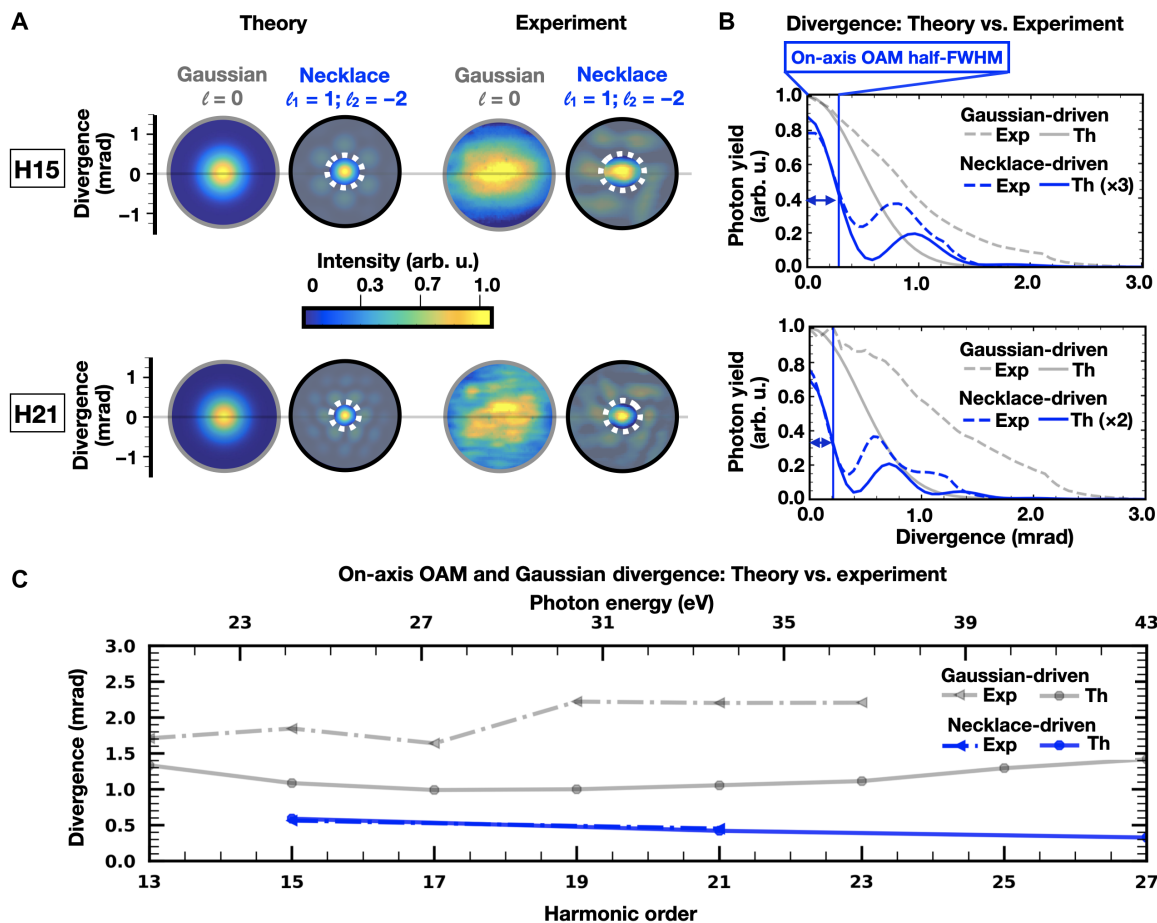
Fig. 5. Ar-driven harmonic divergences. (A) Theoretical (Th) and experimental (Exp) comparison of the intensity spatial profiles for the 790-nm Gaussian- and necklace-driven ($\ell_1 = 1$ and $\ell_2 = -2$) in Ar gas. The white dashed circles indicate the on-axis emission of the 15th (H15) and 21st (H21) harmonics for both theory and experiment. We applied an angular integration radially to these profiles to extract the divergences. **(B)** Angularly integrated radial profiles for H15 and H21 for the on-axis emission, necklace-driven case compared to the equivalent Gaussian. The vertical blue line and double-headed arrow indicate half of the FWHM of the dual-vortex, necklace-driven profile. The intensities of the theoretically predicted on-axis divergence are rescaled for H15 and H21, respectively, to match the intensities of the experimental profiles. **(C)** Theoretical (Eq. 5) and measured FWHM for necklace-driven on-axis emission profile indicates a decrease in the divergence with increasing harmonic order. This is in contrast to Gaussian-driven HHG, where divergence increases at higher harmonic orders.

DISCUSSION

Our results present a notable advance for applications that require highly coherent EUV/SXR beams with customizable properties. By changing the OAM content and radius of the necklace driving field, one can adjust on-demand the line spacing and divergence behavior, respectively, of the emitted high-harmonic combs to tailor the light source for a particular application. Necklace-driven HHG thus enables marked control over the HHG spectra without altering the wavelength of the driving laser. The spectral control instead arises as a result of OAM conservation and macroscopic transverse phase-matching conditions—the microscopic HHG physics remains unchanged, thus avoiding trade-offs in cutoff energy or conversion efficiency. Specifically, under the strong-field approximation, the cutoff energy fulfills the standard rule, $E_{cutoff} = I_p + 3.17 U_p$, where I_p is the ionization energy and U_p is the ponderomotive energy (*52*). The ability to adjust the spacing between harmonic orders enhances the flexibility of HHG light sources for a variety of applications, particularly in the SXR region, when driven by mid-IR

lasers. We note that our necklace-driven HHG scheme allows us to adjust the peak spacing, which, when combined with tunable mid-IR laser drivers that can precisely control the peak position, allows for tailoring of the HHG comb for applications.

In addition to the potential advantages of the unique spectral properties, the needle-like divergence behavior of the harmonics generated in our scheme may enable a simplification of selected imaging and spectroscopy experiments by removing the need for either refocusing optics or methods to eliminate the driving laser beam. Instead, the on-axis contribution of the OAM harmonics could be selected through a pinhole spatial filter, transmitting the full on-axis EUV/SXR flux while blocking the driving laser. Although this might not be sufficient for all applications of EUV/SXR sources, we note that the divergence could be further reduced by adjusting the size of the driving beam—see Eq. 5 and fig. S2—at a cost of driving pulse energy. This possibility offered by phased-necklace drivers is particularly true at shorter wavelengths due to the unique divergence scaling—since the divergence decreases monotonically with

increasing photon energy. This result is especially relevant for HHG driven by mid-IR lasers, where harmonics up to the 1000th can be obtained (see Fig. 2C) for a 2-μm driving laser, extending well into the SXR region. Given the challenge of fabricating and aligning SXR beams, many experiments could directly use these low-divergence necklace-driven HHG beams. We do not foresee any fundamental restriction to applying this technique to even longer driving wavelengths (22, 53), making it possible to tailor very high order discrete harmonics with extremely low divergence.

In conclusion, we have presented a original technique for the generation of EUV and SXR harmonic combs with a line spacing that is controlled through the OAM makeup of IR necklace driving laser beams. The emitted harmonics exhibit low divergence, which further decreases with the harmonic order, in contrast to standard HHG driven by a Gaussian beam. This can enable simpler experimental setups for SXR spectroscopies. Our theoretical simulations are corroborated by our experimental results, which demonstrate both the frequency control and divergence behavior of the generated harmonic combs. Our work will facilitate a variety of applications that require high beam quality and spectroscopic precision, such as tabletop soft x-ray angle resolved photoelectron spectroscopy (SXR-ARPES) or resonant magnetic scattering. The ability to adjust and maintain separation between adjacent harmonic orders is also likely to be beneficial for hyperspectral coherent diffractive imaging techniques (54, 55), particularly in the SXR region. The low divergence and high beam quality enable these experiments to be carried out with simplified setups and enhanced flux throughput. Thus, we believe that necklace-driven HHG will become a powerful tool for tabletop EUV/SXR spectroscopy and imaging, as well as measurements of ultrafast charge and spin dynamics at the nanoscale.

METHODS
Theoretical simulations of HHG driven by a combination of OAM beams
We use a theoretical method that computes both the full quantum single-atom HHG response and subsequent propagation (49), thus taking into account phase matching of the high-order harmonics generated in the gas jet. On the one hand, the quantum single-atom response is reproduced by calculating the dipole acceleration through the full quantum extended strong field approximation—without performing the saddle-point approximation—which presents an excellent qualitative and quantitative agreement against the time-dependent Schrödinger equation. Such approximation allows us to achieve substantial computational time gain when computing macroscopic HHG over the entire gas jet. On the other hand, harmonic propagation and phase matching are computed through the electromagnetic field propagator (49). We discretize the target (gas jet) into elementary radiators, assuming that the emitted harmonic radiation propagates with the vacuum phase velocity. In the present simulations, we have assumed an infinitely thin gas jet, flowing along the perpendicular direction to the beam propagation, with a peak pressure of 667 Pa (5 torr). We note that such 2D assumption for the gas target—performed due to computational time limitations—where only transverse phase matching is considered, is a reasonable assumption for low-density gas jets, based on previous theoretical and experimental results (20, 21). Thus, we do not foresee fundamental deviations if thicker gas jets, closer to the experimental one (150 μm in diameter), are considered.

The spatial structure of the driving beams is represented as a Laguerre-Gaussian beam propagating in the z direction, with wavelength λ_0 ($k_0 = 2\pi/\lambda_0$) given by

$$
\begin{aligned}
\mathrm{LG}_{\ell,p}\,(\rho,\theta,z;k_0) &= E_0 \frac{w_0}{w(z)} \left(\frac{\sqrt{2}\,\rho}{w(z)} \right)^{|\ell|} L_p^{|\ell|} \left(\frac{2\rho^2}{w^2(z)} \right) \\
&\times \exp\left[-\frac{\rho^2}{w^2(z)} \right] \exp\left[i\ell\theta + i\frac{k_0\rho^2}{2R(z)} + i\phi_G(z) \right]
\end{aligned}
\tag{6}
$$

where $w(z) = w_0\sqrt{1 + (z/z_0)^2}$ is the beam waist (with w_0 being the beam waist at focus and $z_0 = \pi w_0^2/\lambda_0$ the Rayleigh range), $R(z) = z[1 + (z_0/z)^2]$ is the phase-front radius, $\phi_G(z) = -(2p + |\ell| + 1)\arctan(z/z_0)$ is the Gouy phase, and $L_p^{|\ell|}(x)$ are the associated Laguerre polynomials. $\ell = 0, \pm1, \pm2\dots$ and $p = 0, 1, 2\dots$ correspond to the topological charge and the number of nonaxial radial nodes of the mode, respectively. In this work, we will not consider beams with radial nodes, and thus, $p = 0$. The driving beam waists (w_0) of the different ℓ modes are chosen to overlap at the focal plane, which corresponds to w_0, $w_0/\sqrt{2}$, $w_0/\sqrt{3}$, $w_0/2$, and $w_0/\sqrt{5}$ for $\ell = \pm1, \pm2, \pm3, \pm4$, and ±5, respectively. In particular, we have considered $w_0 = 30$ μm. Last, the laser pulses are modeled with a trapezoidal envelope. In the simulations performed in Ar and He with 800-nm central wavelength, the envelope consists of 3 cycles of $\sin^2$ turn-on, 10 cycles of constant amplitude (26.7 fs), and 3 cycles of $\sin^2$ turn-off. In the simulations performed in He with 2-μm central wavelength, the pulse duration is reduced due to computational time restrictions, and the envelope consists of two cycles of $\sin^2$ turn-on, four cycles of constant amplitude (26.7 fs), and two cycles of $\sin^2$ turn-off. The amplitudes (E_0) of the driving pulses are chosen to obtain a maximum peak intensity at focus at the radii of maximum superposition ($w_0/\sqrt{2}$) of 1.7×10^{14} W/cm² for Ar, 6.9×10^{14} W/cm² for He at 800 nm, and 5×10^{14} W/cm² for He at 2 μm. Note that the intensity ratio for each Laguerre-Gaussian combination has been chosen to optimize the harmonic radiation emitted around the beam axis (see the Supplementary Materials).

Experimental generation
Necklace beam–driven high harmonics are generated by focusing a pair of collinear, linearly polarized IR-vortex beams (with topological charges of $\ell_1 = 1$, $\ell_2 = -2$) into a supersonic expansion of argon gas. The dual-vortex driver is synthesized from the output of a high-power, ultrafast regenerative amplifier (790 nm, 40 fs, 8 mJ, 1 kHz, KMLabs Wyvern HE) passed through a frequency degenerate Mach-Zehnder interferometer. In each arm of the interferometer, independent spiral phase plates (16 steps per phase ramp, HoloOr) and focusing lenses ($f_1 = 40$ cm, $f_{-2} = 30$ cm) result in each beam with identical (linear) polarization, distinct topological charges, and similarly sized spatial profiles at focus. Independent irises allow for fine tuning of the transverse mode size at the focal plane and are used to overlap the maximum intensity ring of the two component beams. The ring of maximum intensity of the two driving beams was matched at a radius of ~32 μm (see the Supplementary Materials). Half-waveplate/polarizer pairs are used to independently adjust the pulse energy in each arm to optimize the on-axis intensity. For the data presented here, the pulse energies are set to $E_1 = 480$ μJ and $E_2 = 290$ μJ. The combined necklace driver is characterized by a modified Gerchberg-Saxton phase retrieval algorithm, which solves for the spatial phase of the composite electric field and allows

confirmation of the desired OAM content of the driving IR field, while additionally confirming the high stability of the interferometer setup (see the Supplementary Materials). The two component pulses experience approximately equal dispersion throughout each arm of the interferometer and are confirmed through frequency-resolved optical gating (FROG) measurements to have equal pulse widths $\tau \approx 57$ fs. A high-precision, high-stability translation stage (Newport, XMS-160S) is used to synchronize the two pulses in time. The beams are recombined at the output of the interferometer and focused into the supersonic expansion of argon from a circular gas jet (150 μm diameter). The generated high harmonics, which range in photon energy from 20 to 35 eV, are transmitted through a 200-nm-thick aluminum filter (Luxel), which serves to block the residual IR driver. The transmitted harmonics are subsequently focused by a toroidal mirror (f_{eff} = 27 cm) and dispersed by a plane ruled EUV grating (1200 grooves/mm, Richardson) at an incidence angle $\theta_{inc} \approx 45°$. The high incidence angle is chosen to balance the dispersion and imaging quality of the spectrometer. An EUV CCD camera (Andor Newton 940) is placed behind the toroidal focal plane so as to image the far field (20 cm from the gas jet) of the dispersed harmonics with a magnification of 1.67. A removable circular pinhole (200 μm diameter) is placed on the optical axis at a distance of 60 cm from the generation region to spatially filter for the on-axis frequency comb. The pinhole functions to transmit only the on-axis harmonics, which develop very slight diffraction rings but propagate otherwise normally through the spectrometer. These parameters are used to calculate the divergence of the produced harmonics. A 100-nm titanium filter (Lebow) with an absorption edge before the 21st harmonic (33 eV) is used to verify the photon energies of the harmonics exhibiting on-axis intensity.

SUPPLEMENTARY MATERIALS
Supplementary material for this article is available at https://science.org/doi/10.1126/sciadv.abj7380

REFERENCES AND NOTES
1. J. Miao, T. Ishikawa, I. K. Robinson, M. Murnane, Beyond crystallography: Diffractive imaging using coherent x-ray light sources. *Science* **348**, 530–535 (2015).
2. Z. Tao, C. Chen, T. Szilvasi, M. Keller, M. Manos, H. Kapteyn, M. Murnane, Direct time-domain observation of attosecond final-state lifetimes in photoemission from solids. *Science* **353**, 62–67 (2016).
3. J. A. Van Bokhoven, C. Lamberti, *X-Ray Absorption and X-Ray Emission Spectroscopy: Theory and Applications* (John Wiley & Sons, 2016).
4. Y. Pertot, S. Cédric, M. Matthews, A. Chauvet, M. Huppert, V. Svoboda, A. von Conta, A. Tehlar, D. Baykusheva, J.-P. Wolf, H. J. Wörner, Time-resolved X-ray absorption spectroscopy with a water window high-harmonic source. *Science* **355**, 264–267 (2017).
5. Y. Zhang, X. Shi, W. You, Z. Tao, Y. Zhong, F. C. Kabeer, P. Maldonado, P. M. Oppeneer, M. Bauer, K. Rossnagel, H. Kapteyn, M. Murnane, Coherent modulation of the electron temperature and electron-phonon couplings in a 2D material. *Proc. Natl. Acad. Sci. U.S.A.* **117**, 8788–8793 (2020).
6. P. Emma, R. Akre, J. Arthur, R. Bionta, C. Bostedt, J. Bozek, A. Brachmann, P. Bucksbaum, R. Coffee, F.-J. Decker, Y. Ding, D. Dowell, S. Edstrom, A. Fisher, J. Frisch, S. Gilevich, J. Hastings, G. Hays, P. Hering, Z. Huang, R. Iverson, H. Loos, M. Messerschmidt, A. Miahnahri, S. Moeller, H.-D. Nuhn, G. Pile, D. Ratner, J. Rzepiela, D. Schultz, T. Smith, P. Stefan, H. Tompkins, J. Turner, J. Welch, W. White, J. Wu, G. Yocky, J. Galayda, First lasing and operation of an ångstrom-wavelength free-electron laser. *Nat. Photonics* **4**, 641–647 (2010).
7. T. Ishikawa, H. Aoyagi, T. Asaka, Y. Asano, N. Azumi, T. Bizen, H. Ego, K. Fukami, T. Fukui, Y. Furukawa, S. Goto, H. Hanaki, T. Hara, T. Hasegawa, T. Hatsui, A. Higashiya, T. Hirono, N. Hosoda, M. Ishii, T. Inagaki, Y. Inubushi, T. Itoga, Y. Joti, M. Kago, T. Kameshima, H. Kimura, Y. Kirihara, G. Kiyomichi, T. Kobayashi, C. Kondo, T. Kudo, H. Maesaka, X. M. Maréchal, T. Masuda, T. Matsushita, S. Matsui, M. Nagasono, N. Nariyama, H. Ohashi, T. Ohata, T. Ohshima, S. Ono, Y. Otake, C. Saji, T. Sakurai, T. Sato, K. Sawada, T. Seike, K. Shirasawa, T. Sugimoto, S. Suzuki, S. Takahashi, H. Takebe,

K. Taheshita, K. Tamasaku, H. Tanaka, R. Tanaka, T. Tanaka, T. Togashi, K. Togawa, A. Tokuhisa, H. Tomizawa, K. Tono, S. Wu, M. Yabashi, M. Yamaga, A. Yamashita, K. Yanagida, C. Zhang, T. Shintake, H. Kitamura, N. Kumagai, A compact X-ray free-electron laser emitting in the sub-ångström region. *Nat. Photonics* **6**, 540–544 (2012).
8. A. McPherson, G. Gibson, H. Jara, U. Johann, T. S. Luk, I. A. McIntyre, K. Boyer, C. K. Rhodes, Studies of multiphoton production of vacuum-ultraviolet radiation in the rare gases. *J. Opt. Soc. Am. B* **4**, 595 (1987).
9. M. Ferray, A. L'Huillier, X. F. Li, L. A. Lompre, G. Mainfray, C. Manus, Multiple-harmonic conversion of 1064-nm radiation in rare gases. *J. Phys. B* **21**, L31–L35 (1988).
10. A. Rundquist, C. G. Durfee III, Z. Chang, C. Herne, S. Backus, M. M. Murnane, H. C. Kapteyn, Phase-matched generation of coherent soft x-rays. *Science* **280**, 1412–1415 (1998).
11. R. A. Bartels, A. Paul, H. Green, H. C. Kapteyn, M. M. Murnane, S. Backus, I. P. Christov, Y. Liu, A. Attwood, C. Jacobsen, Generation of spatially coherent light at extreme ultraviolet wavelengths. *Science* **297**, 376–378 (2002).
12. P. Agostini, L. F. DiMauro, The physics of attosecond light pulses. *Rep. Prog. Phys.* **67**, 813–855 (2004).
13. T. Popmintchev, M.-C. Chen, P. Arpin, M. M. Murnane, H. C. Kapteyn, The attosecond nonlinear optics of bright coherent X-ray generation. *Nat. Photonics* **4**, 822–832 (2010).
14. F. Calegari, G. Sansone, S. Stagira, C. Vozzi, M. Nisoli, Advances in attosecond science. *J. Phys. B* **49**, 062001 (2016).
15. H. Eichmann, A. Egbert, S. Nolte, C. Momma, B. Wellegehausen, W. Becker, S. Long, J. K. McIver, Polarization-dependent high-order two-color mixing. *Phys. Rev. A* **51**, R3414–R3417 (1995).
16. Z. Chang, A. Rundquist, H. Wang, H. Kapteyn, M. M. Murnane, Temporal phase control of soft-X-ray harmonic emission. *Phys. Rev. A Rapid Commun.* **58**, R30–R33 (1998).
17. R. Bartels, S. Backus, E. Zeek, L. Misoguti, G. Vdovin, I. P. Christov, M. M. Murnane, H. C. Kapteyn, Shaped-pulse optimization of coherent emission of high-harmonic soft X-rays. *Nature* **406**, 164–166 (2000).
18. T. Fan, P. Grychtol, T. Knut, C. Hernández-García, D. D. Hickstein, D. Zusin, C. Gentry, F. J. Dollar, C. A. Mancuso, C. W. Hogle, O. Kfir, D. Legut, K. Carva, J. L. Ellis, K. M. Dorney, C. Chen, O. G. Shpyrko, E. E. Fullerton, O. Cohen, P. M. Oppeneer, D. B. Milošević, A. Becker, A. Jaroń-Becker, T. Popmintchev, M. M. Murnane, H. C. Kapteyn, Bright circularly polarized soft X-ray high harmonics for x-ray magnetic circular dichroism. *Proc. Natl. Acad. Sci. U.S.A.* **112**, 14206–14211 (2015).
19. D. D. Hickstein, F. J. Dollar, P. Grychtol, J. L. Ellis, R. Knut, C. Hernández-García, D. Zusin, C. Gentry, J. M. Shaw, T. Fan, K. M. Dorney, A. Becker, A. Jaroń-Becker, H. C. Kapteyn, M. M. Murnane, C. G. Durfee, Non-collinear generation of angularly isolated circularly polarized high harmonics. *Nat. Photonics* **9**, 743–750 (2015).
20. K. M. Dorney, L. Rego, N. J. Brooks, J. San Román, C.-T. Liao, J. L. Ellis, D. Zusin, C. Gentry, Q. L. Nguyen, J. M. Shaw, A. Picón, L. Plaja, H. C. Kapteyn, M. M. Murnane, C. Hernández-García, Controlling the polarization and vortex charge of attosecond high-harmonic beams via simultaneous spin-orbit momentum conservation. *Nat. Photonics* **13**, 123–130 (2019).
21. L. Rego, K. M. Dorney, N. J. Brooks, Q. L. Nguyen, C.-T. Liao, J. San Román, D. E. Couch, A. Liu, E. Pisanty, M. Lewenstein, L. Plaja, H. C. Kapteyn, M. M. Murnane, C. Hernández-García, Generation of extreme-ultraviolet beams with time-varying orbital angular momentum. *Science* **364**, eaaw9486 (2019).
22. T. Popmintchev, M.-C. Chen, D. Popmintchev, P. Arpin, S. Brown, S. Ališauskas, G. Andriukaitis, T. Balčiunas, O. D. Mücke, A. Pugzlys, A. Baltuška, B. Shim, S. E. Schrauth, A. Gaeta, C. Hernández-García, L. Plaja, A. Becker, A. Jaroń-Becker, M. M. Murnane, H. C. Kapteyn, Bright coherent ultrahigh harmonics in the keV X-ray regime from mid-infrared femtosecond lasers. *Science* **336**, 1287–1291 (2012).
23. D. Popmintchev, C. Hernández-García, F. Dollar, C. Mancuso, J. A. Pérez-Hernández, M.-C. Chen, A. Hankla, X. Gao, B. Shim, A. L. Gaeta, M. Tarazkar, D. A. Romanov, R. J. Levis, J. A. Gaffney, M. Foord, S. B. Libby, A. Jaron-Becker, A. Becker, L. Plaja, M. M. Murnane, H. C. Kapteyn, T. Popmintchev, Ultraviolet surprise: Efficient soft x-ray high-harmonic generation in multiply-ionized plasmas. *Science* **350**, 1225–1231 (2015).
24. Z. Chang, A. Rundquist, H. Wang, M. M. Murnane, H. C. Kapteyn, Generation of coherent X-rays at 2.7nm using high harmonic generation. *Phys. Rev. Lett.* **79**, 2967–2970 (1997).
25. C. Spielmann, N. H. Burnett, S. Sartania, R. Koppitsch, M. Schnürer, C. Kan, M. Lenzner, P. Wobrauschek, F. Krausz, Generation of coherent X-rays in the water window using 5-femtosecond laser pulses. *Science* **278**, 661–664 (1997).
26. E. J. Takahashi, T. Kanai, K. L. Ishikawa, Y. Nabekawa, K. Midorikawa, Coherent water window X ray by phase-matched high-order harmonic generation in neutral media. *Phys. Rev. Lett.* **101**, 253901 (2008).
27. M.-C. Chen, P. Arpin, T. Popmintchev, M. Gerrity, B. Zhang, M. Seaberg, D. Popmintchev, M. M. Murnane, H. C. Kapteyn, Bright, coherent, ultrafast soft X-ray harmonics spanning the water window from a tabletop light source. *Phys. Rev. Lett.* **105**, 173901 (2010).
28. S. M. Teichmann, F. Silva, S. L. Cousin, M. Hemmer, J. Biegert, 0.5-keV Soft X-ray attosecond continua. *Nat. Commun.* **7**, 11493 (2016).
29. A. S. Johnson, D. R. Austin, D. A. Wood, C. Brahms, A. Gregory, K. B. Holzner, S. Jarosch, E. W. Larsen, S. Parker, C. S. Strüber, P. Ye, J. W. G. Tisch, J. P. Marangos, High-flux soft

X-ray harmonic generation from ionization-shaped few-cycle laser pulses. *Sci. Adv.* **4**, eaar3761 (2018).

30. J. Schötz, B. Förg, W. Schweinberger, I. Liontos, H. A. Masood, A. M. Kamal, C. Jakubeit, N. G. Kling, T. Paasch-Colberg, S. Biswas, M. Högner, I. Pupeza, M. Alharbi, A. M. Azzeer, M. F. Kling, Phase-matching for generation of isolated attosecond XUV and soft-X-ray pulses with few-cycle drivers. *Phys. Rev. X* **10**, 041011 (2020).

31. H. Wikmark, C. Guo, J. Vogelsang, P. W. Smorenburg, H. Coudert-Alteirac, J. Lahl, J. Peschel, P. Rudawski, H. Dacasa, S. Carlström, S. Maclot, M. B. Gaarde, P. Johnsson, C. L. Arnold, A. L'Huillier, Spatiotemporal coupling of attosecond pulses. *Proc. Natl. Acad. Sci. U.S.A.* **116**, 4779–4787 (2019).

32. L. Quintard, V. Strelkov, J. Vabek, O. Hort, A. Dubrouil, D. Descamps, F. Burgy, C. Péjot, E. Mével, E. Catoire, E. Constant, Optics-less focusing of XUV high-order harmonics. *Adv. Sci.* **5**, eaau7175 (2019).

33. H. Rubinsztein-Dunlop, A. Forbes, M. V. Berry, M. R. Dennis, D. L. Andrews, M. Mansuripur, C. Denz, C. Alpmann, P. Banzer, T. Bauer, E. Karimi, L. Marrucci, M. Padgett, M. Ritsch-Marte, N. M. Litchinitser, N. P. Bigelow, C. Rosales-Guzmán, A. Belmonte, J. P. Torres, T. W. Neely, M. Baker, R. Gordon, A. B. Stilgoe, J. Romero, A. G. White, R. Fickler, A. E. Willner, G. Xie, B. McMorran, A. M. Weiner, Roadmap on structured light. *J. Opt.* **19**, 013001 (2017).

34. R. A. Beth, Mechanical detection and measurement of the angular momentum of light. *Phys. Rev.* **50**, 115–125 (1936).

35. A. Allen, M. W. Beijersbergen, R. J. C. Spreeuw, J. P. Woerdman, Orbital angular momentum of light and the transformation of Laguerre-Gaussian laser modes. *Phys. Rev. A* **45**, 8185–8189 (1992).

36. M. Zürch, C. Kern, P. Hansinger, A. Dreischuh, C. Spielmann, Strong-field physics with singular light beams. *Nat. Phys.* **8**, 743–746 (2012).

37. C. Hernández-García, A. Picón, J. San Román, L. Plaja, Attosecond extreme ultraviolet vortices from high-order harmonic generation. *Phys. Rev. Lett.* **111**, 083602 (2013).

38. G. Gariepy, J. Leach, K. T. Kim, T. J. Hammond, E. Frumker, R. W. Boyd, P. B. Corkum, Creating high-harmonic beams with controlled orbital angular momentum. *Phys. Rev. Lett.* **113**, 153901 (2014).

39. R. Géneaux, A. Camper, T. Auguste, O. Gobert, J. Caillat, R. Taïeb, T. Ruchon, Synthesis and characterization of attosecond light vortices in the extreme ultraviolet. *Nat. Commun.* **7**, 12583 (2016).

40. L. Rego, J. San Román, A. Picón, L. Plaja, C. Hernández-García, Nonperturbative twist in the generation of extreme-ultraviolet vortex beams. *Phys. Rev. Lett.* **117**, 163202 (2016).

41. F. Kong, C. Zhang, F. Bouchard, Z. Li, G. G. Brown, D. H. Ko, T. J. Hammond, L. Arissian, R. W. Boyd, E. Karimi, P. B. Corkum, Controlling the orbital angular momentum of high harmonic vortices. *Nat. Commun.* **8**, 14970 (2017).

42. D. Gauthier, P. Rebernik Ribic, G. Adhikary, A. Camper, C. Chappuis, R. Cucini, L. F. DiMauro, G. Dovillaire, F. Frassetto, R. Géneaux, P. Miotti, L. Poletto, B. Ressel, C. Spezzani, M. Stupar, T. Ruchon, G. De Ninno, Tunable orbital angular momentum in high-harmonic generation. *Nat. Commun.* **8**, 14971 (2017).

43. L. Rego, J. San Román, L. Plaja, C. Hernández-García, Trains of attosecond pulses structured with time-ordered polarization states. *Opt. Lett.* **45**, 5636–5639 (2020).

44. M. Soljačić, S. Sears, M. Segev, Self-trapping of "necklace" beams in self-focusing Kerr media. *Phys. Rev. Lett.* **81**, 4851–4854 (1998).

45. W. Walasik, S. Z. Silahli, N. M. Litchinitser, Dynamics of necklace beams in nonlinear colloidal suspensions. *Sci. Rep.* **7**, 11709 (2017).

46. L. Zhu, J. Wang, Arbitrary manipulation of spatial amplitude and phase using phase-only spatial light modulators. *Sci. Rep.* **4**, 7441 (2014).

47. T. D. Grow, A. A. Ishaaya, L. T. Vuong, A. L. Gaeta, Collapse and stability of necklace beams in Kerr media. *Phys. Rev. Lett.* **99**, 133902 (2007).

48. J. C. T. Lee, S. J. Alexander, S. D. Kevan, S. Roy, M. J. McMorran, Laguerre-gauss and hermite-gauss soft X-ray states generated using diffractive optics. *Nat. Photonics* **13**, 205–209 (2019).

49. C. Hernández-García, C. J. A. Pérez-Hernández, J. Ramos, E. Conejero Jarque, L. Roso, L. Plaja, High-order harmonic propagation in gases within the discrete dipole approximation. *Phys. Rev. A* **82**, 0033432 (2010).

50. D. Baykusheva, D. Zindel, V. Svoboda, E. Bommeli, M. Ochsner, A. Tehlar, H. J. Wörner, Real-time probing of chirality during a chemical reaction. *Proc. Natl. Acad. Sci. U.S.A.* **116**, 23923–23929 (2019).

51. D. Baykusheva, H. J. Wörner, Chiral discrimination through bielliptical high-harmonic spectroscopy. *Phys. Rev. X* **8**, 031060 (2018).

52. M. Lewenstein, P. Balcou, M. Y. Ivanov, A. L'Huillier, P. B. Corkum, Theory of high-harmonic generation by low-frequency laser fields. *Phys. Rev. A* **49**, 2117–2132 (1994).

53. C. Hernández-García, J. A. Pérez-Hernández, T. Popmintchev, M. M. Murnane, H. C. Kapteyn, A. Jaron-Becker, A. Becker, L. Plaja, Zeptosecond high harmonic keV X-ray waveforms driven by midinfrared laser pulses. *Phys. Rev. Lett.* **111**, 033002 (2013).

54. D. J. Batey, D. Claus, J. M. Rodenburg, Information multiplexing in ptychography. *Ultramicroscopy* **138**, 13–21 (2014).

55. B. Zhang, D. F. Gardner, M. H. Seaberg, E. R. Shanblatt, C. L. Porter, R. Karl, C. A. Mancuso, H. C. Kapteyn, M. M. Murnane, D. E. Adams, Ptychographic hyperspectral spectromicroscopy with an extreme ultraviolet high harmonic comb. *Opt. Express* **24**, 16 (2016).

56. M. Abramowitz, I. A. Stegun, *Handbook of Mathematical Functions with Formulas, Graphs and Mathematical Tables* (Dover, 1966).

57. R. W. Gerchberg, W. O. Saxton, A practical algorithm for the determination of phase from image and diffraction plane pictures. *Optik* **35**, 237–246 (1972).

58. S. Fu, S. Zhang, T. Wang, C. Gao, Pre-turbulence compensation of orbital angular momentum beams based on a probe and the Gerchberg-Saxton algorithm. *Opt. Lett.* **41**, 3185–3188 (2016).

59. H. Chang, X.-L. Yin, X.-Z. Cui, Z.-C. Zhang, J.-X. Ma, G.-H. Wu, L.-J. Zhang, X.-J. Xin, Adaptive optics compensation of orbital angular momentum beams with a modified Gerchberg-Saxton-based phase retrieval algorithm. *Opt. Commun.* **405**, 271–275 (2017).

Science Advances

Necklace-structured high-harmonic generation for low-divergence, soft x-ray harmonic combs with tunable line spacing

Laura RegoNathan J. BrooksQuynh L. D. NguyenJulio San RománIona BinnieLuis PlajaHenry C. KapteynMargaret M. MurnaneCarlos Hernández-García

View the article online
https://www.science.org/doi/10.1126/sciadv.abj7380
Permissions
https://www.science.org/help/reprints-and-permissions

Use of think article is subject to the Terms of service